

Supporting Information Appendix: Meso-scale turbulence in living fluids

Henricus H. Wensink ^{*} [†], Jörn Dunkel [‡], Sebastian Heidenreich [§], Knut Drescher [‡] [¶], Raymond E. Goldstein [‡], Hartmut Löwen ^{*} and Julia M. Yeomans ^{||}

^{*}Institute for Theoretical Physics II: Soft Matter, Heinrich-Heine-Universität Düsseldorf, Universitätsstraße 1, D-40225, Düsseldorf, Germany, [†]Laboratoire de Physique des Solides, Université Paris-Sud 11, Bâtiment 510, 91405 Orsay Cedex, France, [‡]DAMTP, Centre for Mathematical Sciences, University of Cambridge, Wilberforce Road, Cambridge CB3 0WA, UK, [§]Physikalisch-Technische Bundesanstalt, Abbestr. 2-12, 10587 Berlin, Germany, [¶]Departments of Molecular Biology and Mechanical and Aerospace Engineering, Princeton University, Princeton, New Jersey 08544, USA, and ^{||}Rudolf Peierls Centre for Theoretical Physics, University of Oxford, 1 Keble Road, Oxford OX1 3NP, UK

SPR Model

Dynamics. We simulate a system of N rigid rods of length ℓ , moving in a 2D volume A with periodic boundary conditions. Steric rod-rod interactions are represented by a segment model, i.e., each rod is partitioned into n equidistant segments. All segments from different rods interact with each other via a Yukawa potential [1]. The pair potential of two rods α and β , that have orientation unit vectors $\{\hat{\mathbf{u}}^\alpha, \hat{\mathbf{u}}^\beta\}$ and are separated by the center-of-mass distance $\Delta\mathbf{r}^{\alpha\beta}$, is given by

$$U^{\alpha\beta} = \frac{U_0}{n^2} \sum_{i=1}^n \sum_{j=1}^n \frac{\exp(-r_{ij}^{\alpha\beta}/\lambda)}{r_{ij}^{\alpha\beta}}. \quad [1]$$

Here, U_0 is the potential amplitude, λ the screening length, and

$$r_{ij}^{\alpha\beta} = |\Delta\mathbf{r}^{\alpha\beta} + (l_i \hat{\mathbf{u}}^\alpha - l_j \hat{\mathbf{u}}^\beta)| \quad [2]$$

the distance between the i th segment of rod α and the j th segment of rod β , with $l_i \in [-(\ell - \lambda)/2, (\ell - \lambda)/2]$ denoting the position of segment i along the symmetry axis of the rod α . The screening length λ defines the effective diameter of the segments. The ‘shape’ of a rod of length ℓ is then determined by the aspect ratio

$$a = \ell/\lambda. \quad [3]$$

The case $a = 1$ corresponds to a single Yukawa point particle ($n = 1$). For $a > 1$, the number of segments per rod is fixed as $n = 3$ for $1 < a \leq 3$ and $n = \lfloor 9a/8 \rfloor$ for $a > 3$ with $\lfloor \cdot \rfloor$ denoting the nearest integer.

Considering the dynamical regime relevant to microorganisms, we assume that the motion of the SPRs is overdamped due to solvent friction (zero Reynolds number limit $\text{Re} = 0$).

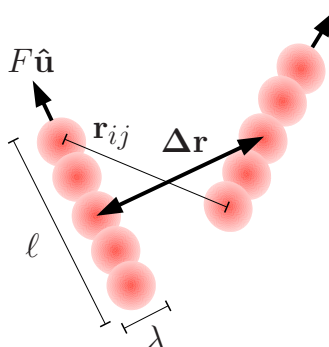


Fig. S1. Sketch of the SPR model. Each rod is represented by $n = 5$ repulsive Yukawa segments and has an aspect ratio $a = \ell/\lambda$. Self-propulsion is provided by a constant force F acting along the main rod axis indicated by the orientational unit vector $\hat{\mathbf{u}}$. The total rod pair potential is obtained by a sum over all Yukawa segment pairs with distance \mathbf{r}_{ij} according to Eq. [1].

Since we are interested in the collision-dominated dynamics in dense bacterial suspensions, we neglect thermal and intrinsic [2] fluctuations of the bacterial orientation and restrict our study to deterministic motions. With these simplifying assumptions, the equations of motion for the center-of-mass $\mathbf{r}_\alpha(t)$ and orientation $\hat{\mathbf{u}}_\alpha(t)$ of an SPR are of first order in time and can be written in the compact form

$$\mathbf{f}_T \cdot \frac{d}{dt} \mathbf{r}_\alpha = F \hat{\mathbf{u}}_\alpha - \nabla_{\mathbf{r}_\alpha} U, \quad [4]$$

$$\mathbf{f}_R \cdot \frac{d}{dt} \hat{\mathbf{u}}_\alpha = -\nabla_{\hat{\mathbf{u}}_\alpha} U. \quad [5]$$

Here, F is a constant self-motility force acting along the longitudinal axis of each rod, $U = (1/2) \sum_{\beta, \alpha: \beta \neq \alpha} U^{\alpha\beta}$ the total potential energy, $\nabla_{\hat{\mathbf{u}}}$ denotes the gradient on the unit circle, and

$$\mathbf{f}_T = f_0 [f_{\parallel} \hat{\mathbf{u}} \hat{\mathbf{u}} + f_{\perp} (\mathbf{I} - \hat{\mathbf{u}} \hat{\mathbf{u}})], \quad [6]$$

$$\mathbf{f}_R = f_0 f_R \mathbf{I} \quad [7]$$

are the translational and rotational friction tensors (\mathbf{I} is the 2D unit tensor) with a Stokesian friction coefficient f_0 . The dimensionless geometric factors $\{f_{\parallel}, f_{\perp}, f_R\}$ depend solely on the aspect ratio a , and we adopt the standard expressions for rod-like macromolecules, as given in Ref. [3]

$$\frac{2\pi}{f_{\parallel}} = \ln a - 0.207 + \frac{0.980}{a} - \frac{0.133}{a^2}, \quad [8]$$

$$\frac{4\pi}{f_{\parallel}} = \ln a + 0.839 + \frac{0.185}{a} + \frac{0.233}{a^2}, \quad [9]$$

$$\frac{\pi a^2}{3f_R} = \ln a - 0.662 + \frac{0.917}{a} - \frac{0.050}{a^2}. \quad [10]$$

We note that after multiplication with the inverse matrix \mathbf{f}_T^{-1} , Eq. [4] can be rewritten as

$$\frac{d}{dt} \mathbf{r}_\alpha = V \hat{\mathbf{u}}_\alpha - \mathbf{f}_T^{-1} \cdot \nabla_{\mathbf{r}_\alpha} U, \quad [11]$$

where

$$V = \frac{F}{f_0 f_{\parallel}} \quad [12]$$

defines the self-swimming speed of a non-interacting SPR. When comparing with dense bacterial suspensions, however, V should be interpreted as an effective parameter that is of the order of the mean self-swimming speed of a bacterium in suspension.

Simulations. In our simulations, we adopted characteristic units such that $\lambda = 1$, $F = 1$, and $f_0 = 1$, which means that distance is measured in units of λ , velocity in units of F/f_0 , time in units of $\lambda f_0/F$ and energy in units of $F\lambda$. Af-

ter rescaling to dimensionless coordinates, three relevant system parameters remain: The dimensionless Yukawa amplitude $\tilde{U}_0 = U_0/(F\lambda)$, which determines the hardness of the rod interactions relative to their characteristic propulsion energy,

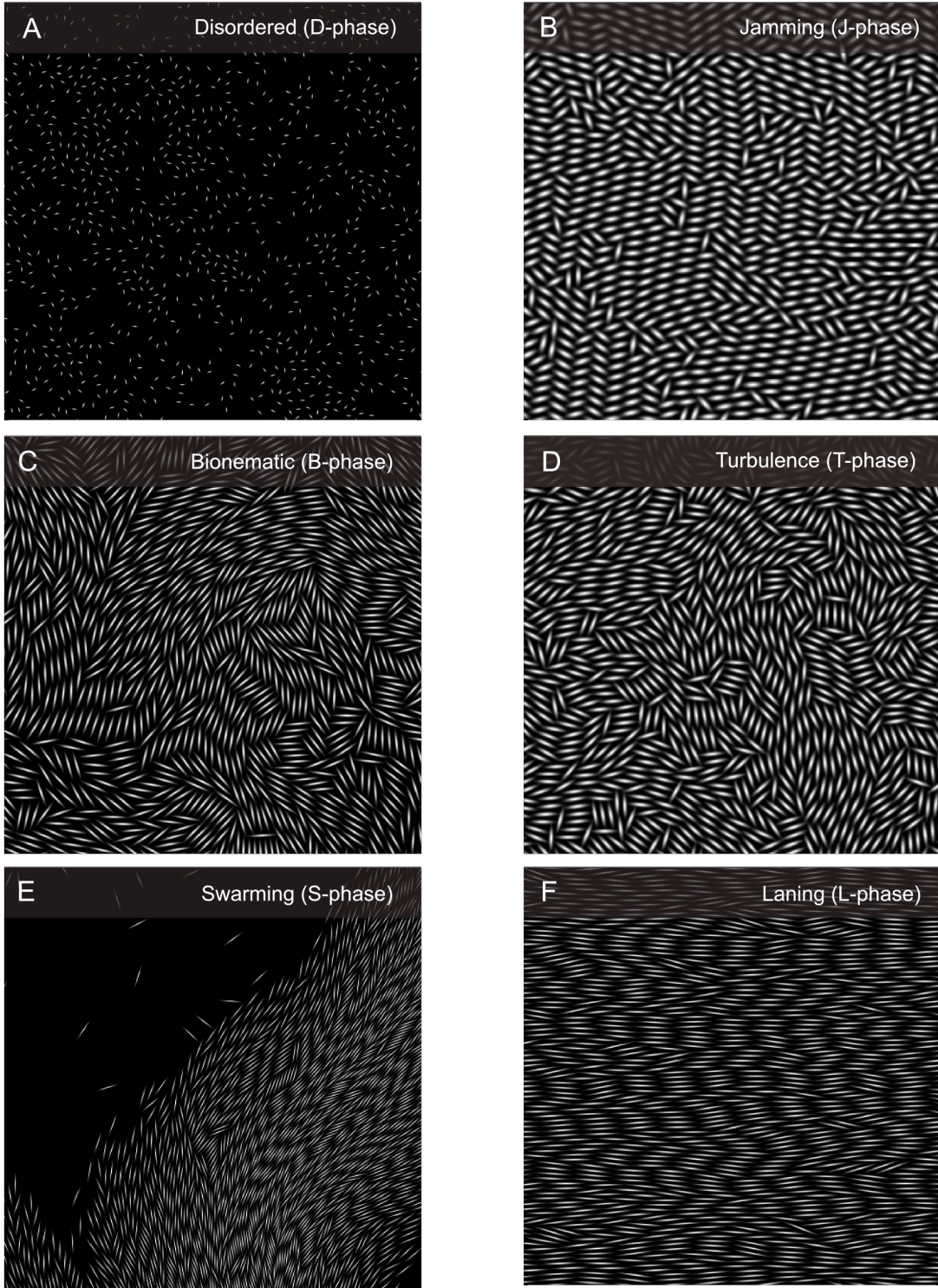


Fig. S2. Snapshots of the different phases of the SPR-model (see also Fig. 1A of the Main Text and Movies S1-S6). Each snapshot shows only a subsection of the full simulation volume, scaled to contain approximately the same mean particle number. Rod-shapes were fitted by elongated Gaussian intensity profiles. Generally, monodisperse SPR phases may exhibit regions of local smectic order (see E,F) that are absent in polydisperse bacterial suspensions. Simulation parameters: (A) particle number $N = 10,000$, aspect ratio $a = 4$, volume fraction $\phi = 0.063$, Yukawa amplitude $U_0 = 250$; (B) $N = 9996$, $a = 3$, $\phi = 0.975$, $U_0 = 250$; (C) $N = 9964$, $a = 9$, $\phi = 0.55$, $U_0 = 250$; (D) $N = 9968$, $a = 5$, $\phi = 0.84$, $U_0 = 250$; (E) $N = 9990$, $a = 16$, $\phi = 0.21$, $U_0 = 250$; (F) $N = 9996$, $a = 16$, $\phi = 0.53$, $U_0 = 250$.

the aspect ratio a , and the effective volume fraction of the system

$$\phi = \frac{N}{A} \left[\lambda(\ell - \lambda) + \frac{\pi\lambda^2}{4} \right], \quad [13]$$

where A is the simulation volume. For sufficiently hard rods, the general dynamical behavior is only weakly dependent on the Yukawa amplitude, and we performed simulations for $\tilde{U}_0 = 250, 455, 500, 555, 625, 1250$. This leaves us with the rod shape a and volume fraction ϕ as the primary parameters. We simulated the evolution of the many-body SPR model as a function of time $\tau = tF/\lambda f_0$ in a square box of length L with periodic boundary conditions at volume fractions in the range $0.05 < \phi < 0.9$. Numerical studies were carried out using a time discretization $\Delta\tau = 0.002\rho^{-1/2}$, where $\rho = N\lambda^2/A$ with typically $N = 10^4 \div 10^5$ rods per simulation. Initial configurations, generated from a rectangular lattice of aligned rods with $\hat{\mathbf{u}}$ pointing randomly up or down were allowed to relax during an interval $\tau = 1000$ before statistics is gathered over an interval $\tau = 20L$ with $L = (N/\rho)^{1/2}$ the dimension of the simulation box (in units of λ). Velocity vector fields $\mathbf{v}(t, \mathbf{r})$ were constructed by measuring the average centre-of-mass velocity within small sub-cells centered around the position \mathbf{r} , as described below.

In order to test for finite size effects, we simulated two different system sizes: ‘small’ systems with $N = 1 \cdot 10^4$ particles and ‘large’ systems with $N = 4 \cdot 10^4$ particles at the same filling fraction ϕ . Generally, we found that statistical quantifiers are robust with respect to changes in the particle number N , provided N is at least of $\mathcal{O}(10^4)$.

Analysis of Simulation Data. The microscopic velocities of the SPRs follow directly from the equations of motion [4] and [5]. From the particle velocities we construct effective flow fields by projecting the particle positions onto a 2D cubic grid $\{(i, j) \mid 1 \leq i, j \leq G\}$ and measuring the average velocity $\mathbf{U}(t; i, j)$ in each bin (i, j) at a given time t . 2D vorticity maps for the SPR model, as shown Fig. 1B and Fig. 2A of the Main Text, were computed from such averaged flow field data. To increase the spatial resolution of the flow field, we allowed neighboring bins to have a 75% overlap (the same overlap was used in the PIV analysis of experimental data, see below). For instance, for a large system $N = 4 \cdot 10^4$ particles and a total box length $L \sim 80\ell$, we used a bin width of $\delta = 1.31\ell$ so that each sub-cell contains approximately 10 rods. In this case, the resulting cubic grid consists of $G \times G = 97 \times 97$ overlapping cells. We verified that the statistical properties of the flow fields remained robust under moderate variations of the bin size. We generally found that results are stable if the bin size is moderately larger than the SPR length $\delta \gtrsim \ell$. However, if the bin size is chosen too large, $\delta \gg \ell$, structural information about vortices is lost.

For the SPR model, statistical quantifiers can be constructed either from the raw particle data or from pre-averaged effective flow fields. Both methods produce qualitatively similar results for the velocity statistics but quantitative differences of several percent are noticeable. Figures 3 and 4 in the Main Text show results that were obtained by direct averaging of individual SPR velocities. The schematic phase diagram and the enstrophy curves in Fig. 1 of the Main Text, and the snapshots in Fig. S2 were computed using a Yukawa amplitude $U_0 = 250$. The SPR results (velocity histograms, structure functions, spectra, etc.) in Figs 2A, 3 and 4 of the Main Text are based on parameters $U_0 = 455$, $a = 5$, $\phi = 0.84$, as these values yield good quantitative agreement with the 2D experimental data.

Number Fluctuations. Additional information about the different dynamical phases of the SPR model can be obtained from the number fluctuations $\Delta N^2 = \langle (N_L - \langle N_L \rangle)^2 \rangle$ of the average number of SPRs $\langle N_L \rangle = NL^2/A$ in a square sub-compartment of linear size L (see Fig S3). From the power-law behaviour $\Delta N \propto \langle N_L \rangle^\gamma$ one can extract an exponent $\gamma = 0.9 \pm 0.2$ which reveal giant fluctuations in the swarming S-phase and bionematic B-phase (note that $\gamma = 0.5$ for a system in thermal equilibrium). The number fluctuations are much weaker for the dilute D-phase although the anomalous exponent ($\gamma \sim 0.6$) hints at some degree of clustering occurring even at low particle density, see also snapshots in Fig. S2. The crossover from S-swarming to T-turbulence in the phase diagram (see Fig. 1A of the Main Text) can be inferred from a steep decrease in the density fluctuations at lower packing fractions. The crossover represents a transition from strongly fluctuating flocking-type flow to homogeneous vortical flow where density fluctuations are suppressed due to packing effects. In particular, the marginal exponent ($\gamma = 0.3$) for the turbulent T-phase supports the assumption of incompressible flow in the continuum theory (see Main Text).

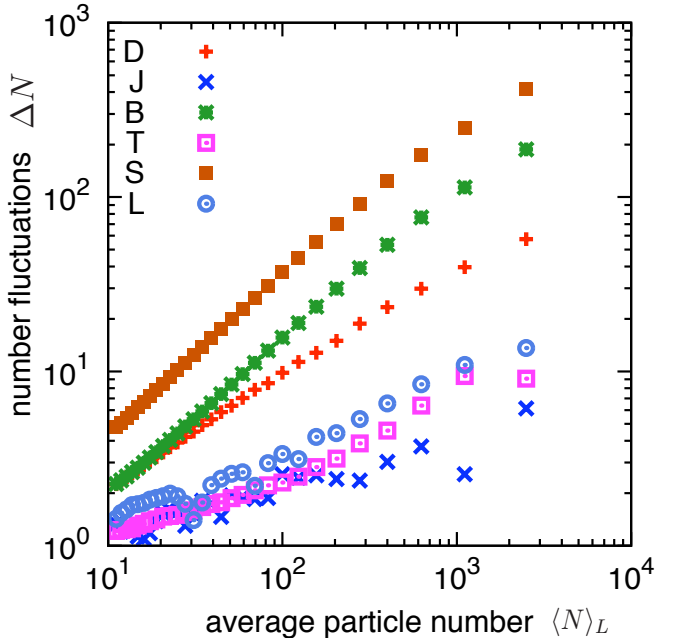


Fig. S3. Typical number fluctuations $\Delta N^2 = \langle (N_L - \langle N_L \rangle)^2 \rangle$ as a function of the average particle number $\langle N_L \rangle$ (see text) for the different emergent states in a system of $N = 10^4$ SPR. The power-law scaling $\Delta N \propto \langle N_L \rangle^\gamma$ reveals giant number fluctuations ($\gamma \sim 1$) for the S-swarming ($a = 16, \phi = 0.21$) and B-bionematic ($a = 9, \phi = 0.55$) phases, while fluctuations are strongly suppressed ($\gamma < 0.5$) in the dense J-jamming ($a = 3, \phi = 0.97$), T-turbulence ($a = 5, \phi = 0.84$) and L-laning ($a = 16, \phi = 0.53$) phases, see also snapshots in Fig. S2. Note that $\gamma = 0.5$ for a system in thermal equilibrium.

Distinction between Turbulent and Bionematic Flow. The defining feature of the ‘zooming’ bionematic phase [4, 5] (here referred to as B-phase) is the existence of jet-like nematic regions, which determine the velocity statistics of the active flow (see Supplementary Movie S3 and also Fig. S2C). At high filling fractions, these jets become suppressed and the system crosses over into a homogeneous turbulent phase (T-phase), as illustrated in the schematic phase diagram (Fig. 1A) of the Main Text.

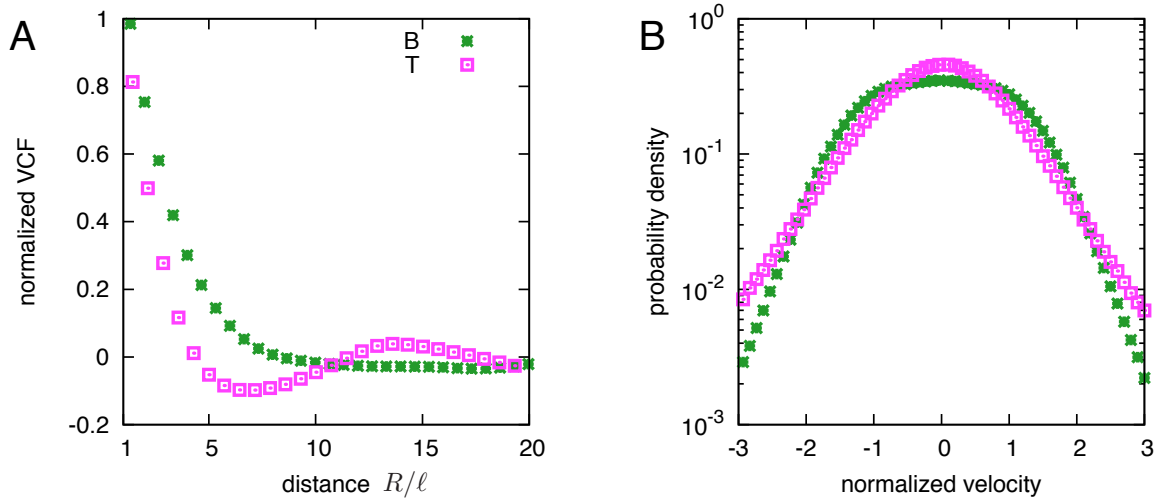


Fig. S4. Comparison of the bionematic B-phase and the turbulent T-phase of the SPR model. (A) Equal-time velocity correlation functions (VCFs), normalised to unity at $R = \ell$, and (B) distribution of the Cartesian velocity components for the B-phase ($a = 9, \phi = 0.55$) and T-turbulence ($a = 5, \phi = 0.84$). The turbulent T-phase exhibits negative velocity correlations that indicate a characteristic vortex size, and the velocity distribution is approximately Gaussian in the central regions with exponential tails. In contrast, the B-phase is characterized by a broadened non-Gaussian shape of the velocity distribution and a flattened VCF.

Statistical quantifiers that can be used to distinguish the B-phase from the T-phase are the velocity correlation function (VCF) and the marginal distribution of the SPR velocities. For the turbulent T-phase, the VCF of shows a clear minimum representing the typical vortex size and the velocity distribution becomes Gaussian in the central regions (see Fig. S4). By contrast, the B-phase is characterized by a strongly non-Gaussian (broadened) shape of the velocity distribution and the oscillations of the VCF are washed out due to existence of bionematic jets (see detailed discussion by Zhang et al. [6]). Furthermore, number fluctuations are much stronger in the B-phase than in the T-phase, as evident from Fig. S3.

Expected Validity and Limitations of the SPR Model. To assess the validity and limitations of the SPR model, it is useful to compare the phases in Fig. S2 with experimental observations reported in the literature [4, 5, 7, 6, 8] and results from our measurements. Representative snapshots of different phases, as observed in our quasi-2D experiments at different bacterial filling fractions, are shown in Fig. S5, see also Supplementary Movies S8-S10.

The dilute D-phase (Fig. S2A and Fig. S5A) was realized in the experiments of Sokolov et al. [7], who also observed the B-phase (Fig. S2C) in *B. subtilis* suspension confined to 2D thin films. The B-phase was also analyzed in detail by Cisneros et al. [4, 5] for *B. subtilis* in 3D open droplets and by Zhang et al. [6] for quasi-2D *Paenibacillus dendritiformis* colonies growing on agar. The correlation functions reported by these authors resemble closely those for the B-phase in the SPR model (Fig. S4). Swarming and flocking states of bacteria, similar to those in Fig. S2E and Fig. S5B, were studied by Zhang et al. [9] and Chen et al. [8] for *B. subtilis* grown on agar. To our knowledge, the jamming phase (Fig. S2B), which corresponds to a ‘frozen’ active crystal, and the laning phase (Fig. S2F) have not yet been realized in experiments with motile bacteria, although recent work by Volfson et al. [10] suggests that it could be possible to observe these phases for sufficiently long bacteria in suitably designed microfluidic chambers.

Generally, we would like to emphasize that, due to their simplicity, SPR models are not likely to capture quantitatively all the details of the bacterial dynamics in semi-dilute suspensions, where collective hydrodynamic effects and intrinsic ori-

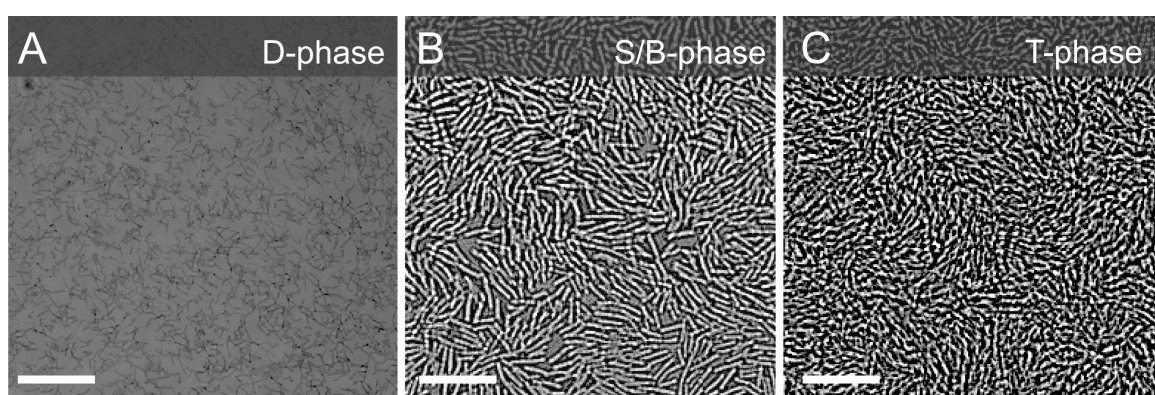


Fig. S5. Micrographs of quasi-2D *B. subtilis* suspensions in the (A) dilute phase at very low filling fractions, (B) near the swarming-bionematic transition at intermediate filling fractions, and (C) in the turbulent regime at very high filling fraction. Scale bars: (A) 30 μm , (B,C) 10 μm . Note the similarities with the corresponding SPR phases in Fig. S2, although some differences exist due to the varying SPR aspect ratios, the polydispersity of bacteria and the fact that the simulations are strictly 2D whereas the microfluidic chamber is only quasi-2D.

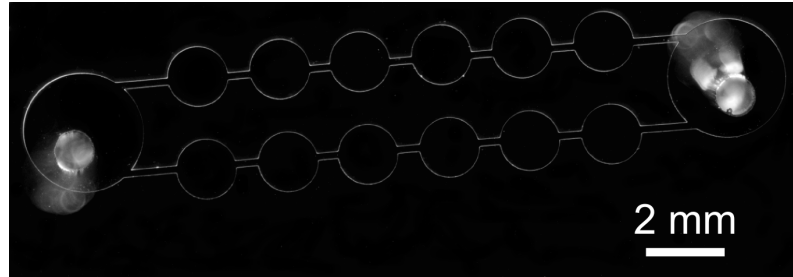


Fig. S6. Dark-field image (top view) of microfluidic chambers as used in the 3D experiments (channel height 80 μm , see also Materials and Methods). Bright spots in the two outer larger chambers are the inlets. Flow field measurements were performed in the small chambers. For the quasi-2D experiments, the same chamber geometry was used but with a reduced channel height of 5 μm .

ential noise in bacterial locomotion [2] become relevant. Deterministic SPR models can be expected to become more accurate the higher the bacterial concentration. This hypothesis appears to be supported by the good agreement for the velocity statistics from our quasi-2D experimental data and 2D SPR data for the T-phase (see Fig. 3 in the Main Text). However, even in the high-density regime, minor quantitative differences between our bacteria experiments and 2D simulations of monodisperse SPR systems are to be expected since (i) our chambers are only approximately 2D and (ii) bacterial suspensions are polydisperse (Fig. S7).

Analysis of Experimental Data

Imaging Parameters. Figure S6 shows microfluidic chambers as used in our experiments (see also Materials and Methods in the Main Text). Microscope images of dense *B. subtilis* suspensions (volume fractions $\phi \sim 0.4$) were recorded at frame rate f , corresponding to a time interval $\Delta t = t_k - t_{k-1} = 1/f$ between subsequent frames $k = 1, \dots, K$. For the quasi-2D experiments we used an image resolution of 700 pix \times 700 pix with conversion rate 0.31 $\mu\text{m}/\text{pix}$ and frame rate $f = 40$ Hz, and for the 3D experiments 768 pix \times 768 pix with 0.29 $\mu\text{m}/\text{pix}$ and $f = 100$ Hz or $f = 200$ Hz.

Estimation of Bacterial Aspect Ratios. The aspect ratios of *B. subtilis* bacteria were determined directly from our imaging data, by analyzing a representative sample (randomly selected 2D layer) of bacteria from a diluted suspension (Fig. S7A). Bacterial shapes were fitted by capped cylinders (Fig. S7B) and the pixel counts were used to determine the histogram shown in Fig. S7C, yielding a mean aspect ratio 6.3 ± 1.2 .

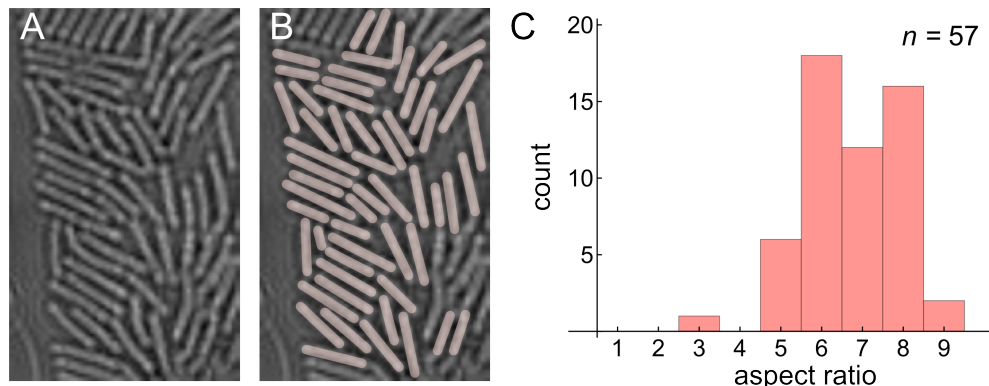


Fig. S7. Estimation of bacterial aspect ratios. (A) Micrograph showing a randomly selected 2D layer from a diluted *B. subtilis* suspension. (B) Bacterial shapes were manually fitted by capped cylinders (pink) and pixel counts were used to obtain the histogram in (C); mean value 6.3 ± 1.2 .

Particle Imaging Velocimetry (PIV). To extract the local flow field components from the experimental movie data, we used the commercial PIV software Dantec Flow Manager. The PIV algorithm estimates the 2D velocity field $\mathbf{U}_P(t_k; i, j)$ at time t_k on a 2D cubic grid. In our analysis, we used averaging windows of size 32 pix \times 32 pix, which roughly corresponds to $2\ell \times 2\ell$ in terms of the mean bacterial length $\ell \sim 4.8 \mu\text{m}$ for *B. subtilis* and is sufficiently large to contain ~ 10 bacteria but still small enough to resolve spatial flow field structures on the order of a few bacterial lengths. The distance between neighboring grid points was chosen to generate a 75% overlap between neighbouring bins. This corresponds to the highest spatial resolution that is achievable within this software for the given window size, resulting in a grid of size $G \times G = 84 \times 84$ for the quasi-2D data, and $G \times G = 93 \times 93$ for the 3D data. A comparison between PIV flow data for quasi-2D and 3D bacterial suspensions is shown in Fig. S8. One readily observes that the typical vortex size is considerably smaller in 2D than in 3D, see also Fig. 4A in the Main Text.

Correction of Systematic Errors. Flow field reconstruction via PIV can introduce systematic errors due to pixel locking (PL) [5]. We correct our flow field data $\mathbf{U}_P(t_k; i, j)$ obtained from the PIV algorithm for PL errors by using a calibration procedure similar to the one that is described in detail in the Appendix of Ref. [5]. The only minor modification adopted here is that, instead of generating a look-up table, we fitted the periodic residual errors by using trigonometric functions which were then used to reconstruct the corrected flow field \mathbf{U} from \mathbf{U}_P . Furthermore, we also corrected \mathbf{U} for small systematic drift effects (e.g., due to weak oxygen gradients caused by the inlets of the microfluidic chambers), by subtracting the

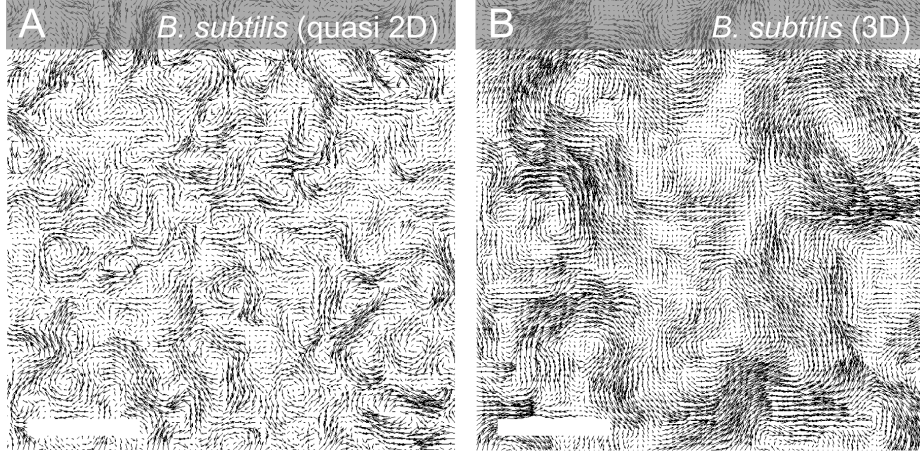


Fig. S8. Snapshots of PIV flow data for dense (A) quasi-2D and (B) 3D *B. subtilis* suspensions. Scale bars 50 μm . Arrow sizes in both diagrams are normalized to the same unit velocity; the maximum velocity in (A) is 26 $\mu\text{m}/\text{s}$. The typical vortex size is considerably smaller in 2D than in 3D, see also Fig. 4A in the Main Text.

mean flow velocity

$$\langle \mathbf{U} \rangle = \frac{1}{K} \sum_{t_k} \langle \mathbf{U}(t_k) \rangle = \frac{1}{K} \sum_{t_k} \frac{1}{G^2} \sum_{i,j} \mathbf{U}(t_k; i, j) \quad [14]$$

from the calibrated data $\mathbf{U}(t_k; i, j)$, yielding the corrected data

$$\mathbf{u}(t_k; i, j) = \mathbf{U}(t_k; i, j) - \langle \mathbf{U} \rangle \quad [15]$$

used in our statistical analysis. The subtraction of the constant $\langle \mathbf{U} \rangle$ does not affect the statistics of velocity increments, but modifies the values obtained for the total kinetic energy or the energy spectrum. Generally, we found that, while the shape of the velocity histograms can be strongly affected by PL effects, the velocity structure functions are not very sensitive (< 1%) to the PL correction.

Continuum Model

We discuss the basic considerations that lead to the continuum model defined by Eq. [1] of the Main Text. This model aims to provide a phenomenological description of quasi-incompressible active fluids by combining elements from the Toner-Tu theory [11, 12] and the Swift-Hohenberg theory [13]. After summarizing the underlying ideas, we will present a linear stability analysis for the 2D case and conclude by commenting on the numerical implementation and parameter choices in our 2D simulations.

Basic Assumptions. Our main objective is to identify a minimal continuum theory that exhibits self-sustained dynamical vortex structures similar to those observed in the SPR simulations and in the *B. subtilis* experiments. To this end, we focus on the limit of very high bacterial concentrations (filling fractions). The model is based on two main assumptions that are guided by insights from the experiments and particle simulations:

1. At sufficiently high concentrations, the bacterial (or SPR) suspension becomes, in good approximation, an incompressible active fluid.
2. The essential dynamics of the bacterial fluid can be captured by a single vectorial order parameter field, the mean flow velocity $\mathbf{v}(t, \mathbf{x})$.

The incompressibility assumption appears to be justified by the fact that density fluctuations are very small in both our experiments and SPR simulations (< 5%), provided the particle density is sufficiently large. The second assumption is

more debatable since, in general, mean velocity and mean orientation of the bacteria could decouple (e.g., if long-range hydrodynamic interactions are important). Our SPR simulations on the other hand suggest that, for very high filling fractions, orientation and velocity are strongly correlated. We therefore expect that the second assumption is reasonable for dense suspensions but becomes invalid at lower concentrations when bacteria assemble into inhomogeneous swarm-like structures [9]. In this flocking regime, see region (S) in Fig. 1A of the Main Text, more complex theories that take into account a locally varying bacterial concentration and distinguish between solvent velocity field, mean bacterial velocity field $\mathbf{v}(t, \mathbf{x})$ and mean bacterial orientation field provide a more adequate description of bacterial suspensions [14, 15, 16]. Another possible extension is the inclusion of additional higher-moment order-parameter fields like the \mathbf{Q} -tensor [17, 18], which encodes local fluctuations in the particle orientations. Due to the very large number of unknown coefficients, however, it seems very difficult if not impossible to constrain such more sophisticated models with the presently available experimental data. Here, we assume that the experimentally observed behavior can be reproduced from a suitably designed theory that only utilizes the flow field \mathbf{v} which can be measured experimentally by PIV or tracking methods.

Field Equations. The incompressibility assumption is implemented by demanding that the flow field $\mathbf{v}(t, \mathbf{x})$ is divergence-free,

$$\nabla \cdot \mathbf{v} = \partial_i v_i = 0, \quad i = 1, \dots, d, \quad [16]$$

where d is the number of space dimensions (throughout, we assume a sum over equal lower indices). We further postulate that the dynamics of \mathbf{v} is governed by a generalized d -dimensional Navier-Stokes equation of the form

$$(\partial_t + \mathbf{v} \cdot \nabla) \mathbf{v} = -\nabla p - (\alpha + \beta |\mathbf{v}|^2) \mathbf{v} + \nabla \cdot \mathbf{E}, \quad [17]$$

where the pressure p is the Lagrange multiplier for the incompressibility condition, α and β are parameters, and the rate-of-strain tensor \mathbf{E} depends on \mathbf{v} as specified below.

The second contribution on the rhs. of Eq. [17] is a typical local driving term as known from the Toner-Tu model [11, 12]. This term effectively corresponds to a quartic Landau-potential for the velocity order-parameter field \mathbf{v} . Stability requires that $\beta \geq 0$, while α is allowed to take positive or negative values. In the absence of other driving mechanisms, the Toner-Tu term drives the fluid to an isotropic

equilibrium state with $\mathbf{v} = 0$ if $\alpha > 0$, whereas for $\alpha < 0$ and $\beta > 0$ the velocity potential becomes ‘bistable’, leading to global polar ordering with characteristic speed

$$v_0 = \sqrt{|\alpha|/\beta}. \quad [18]$$

To close the model equations, we still need to specify \mathbf{E} in terms of \mathbf{v} and its derivatives. Using guidance from the theory of active nematics [15], we postulate the components of the symmetric and trace-free rate-of-strain tensor \mathbf{E} to have the form

$$E_{ij} = \Gamma_0(\partial_i v_j + \partial_j v_i) - \Gamma_2 \Delta (\partial_i v_j + \partial_j v_i) + S q_{ij}, \quad [19]$$

where $\Delta = \nabla^2$ is the d -dimensional Laplacian, and

$$q_{ij} = v_i v_j - \frac{\delta_{ij}}{d} |\mathbf{v}|^2 \quad [20]$$

is a mean-field approximation to the Q -tensor (recalling our assumption that the direction of the velocity field coincides with mean local swimmer orientation), with the Kronecker-symbol δ_{ij} denoting elements of the unit matrix \mathbf{I} . For $\Gamma_0 > 0$ and $S = 0 = \Gamma_2$, Eq. [19] reduces to the usual rate-of-strain tensor of a conventional fluid with viscosity Γ_0 . However, to obtain a minimal model of self-sustained turbulence in active suspensions, we shall allow for negative values $\Gamma_0 < 0$ while demanding in this case that $\Gamma_2 > 0$ to ensure stability of the theory (see detailed stability analysis below). The additional S -term in Eq. [19] presents an active stress contribution (in mean-field approximation) as known from theories of active nematics [15]. General hydrodynamic considerations [16] suggest that $S > 0$ for puller-type swimmers (e.g., algae), whereas $S < 0$ for pushers such as *B. subtilis*. Intuitively, one may regard the two Γ -terms in Eq. [19] as arising from a systematic (linear in \mathbf{v}) expansion of the stress-tensor, with the higher-order derivatives (Γ_2 -term) accounting for longer-range multi-particle interactions.

Inserting Eq. [19] into Eq. [17], and defining

$$\lambda_0 = 1 - S, \quad \lambda_1 = -S/d, \quad [21]$$

we obtain

$$\begin{aligned} (\partial_t + \lambda_0 \mathbf{v} \cdot \nabla) \mathbf{v} &= -\nabla p + \lambda_1 \nabla \mathbf{v}^2 - (\alpha + \beta |\mathbf{v}|^2) \mathbf{v} + \\ &\quad \Gamma_0 \Delta \mathbf{v} - \Gamma_2 \Delta^2 \mathbf{v}. \end{aligned} \quad [22]$$

As we shall see below, the two Γ -terms in Eq. [22], which are reminiscent of the higher-order derivatives in the Swift-Hohenberg theory [13], are essential for the formation of quasi-chaotic flow patterns in this model. These linear terms provide a simple (if not the simplest) generic description of turbulent instabilities in dense bacterial suspensions – and the resulting theory agrees remarkably with well both our experiments and particle simulations. More generally, we expect Eq. [22] to provide a satisfactory phenomenological description whenever interaction terms in more complex field theories, that lead to instabilities in the \mathbf{v} -field, can be effectively approximated by a fourth-order Taylor expansion in Fourier space, which is likely to be the case for a wide range of active systems. Phrased differently, the last two terms in Eq. [22] may be regarded as the Fourier-space analogue of the Toner-Tu driving terms, which correspond to a series expansion in terms of the order parameter.

Before presenting a linear stability analysis for the ‘minimal’ continuum model defined by Eqs. [16] and [22], let us still note that it is straightforward to construct extensions of the theory, e.g., by including density fluctuations or coupling to concentration fields.

2D Stability Analysis. We perform a stability analysis for the 2D case relevant to our particle simulations and quasi-2D experiments, assuming that $\Gamma_0 < 0$ and $\beta > 0$, $\Gamma_2 > 0$.

For arbitrary values of α , Eqs. [16] and [22] have a fixed point that corresponds to a disordered isotropic state

$$\mathcal{S}_i : (\mathbf{v}, p) = (\mathbf{0}, p_0), \quad [23]$$

where p_0 is a pressure constant. For $\alpha < 0$, an additional class of fixed points arises, corresponding to a manifold of globally ordered polar states

$$\mathcal{S}_p : (\mathbf{v}, p) = (\mathbf{v}_0, p_0), \quad [24]$$

where \mathbf{v}_0 is constant vector with arbitrary orientation and fixed swimming speed $|\mathbf{v}_0| = \sqrt{|\alpha|/\beta} =: v_0$.

(i) Stability of the disordered isotropic state \mathcal{S}_i . Linearizing Eqs. [16] and [22] for small velocity and pressure perturbations around the isotropic state, $\mathbf{v} = \varepsilon$ and $p = p_0 + \eta$ with $|\eta| \ll |p_0|$, we have to leading order

$$0 = \nabla \cdot \varepsilon, \quad [25]$$

$$\partial_t \varepsilon = -\nabla \eta - \alpha \varepsilon + \Gamma_0 \Delta \varepsilon - \Gamma_2 \Delta^2 \varepsilon. \quad [26]$$

Considering perturbations of the form

$$(\eta, \varepsilon) = (\hat{\eta}, \hat{\varepsilon}) e^{i\mathbf{k} \cdot \mathbf{x} + \sigma t} \quad [27]$$

and defining $k = |\mathbf{k}|$, we find

$$0 = \mathbf{k} \cdot \hat{\varepsilon} \quad [28]$$

$$\sigma \hat{\varepsilon} = -i\hat{\eta} \mathbf{k} - (\alpha + \Gamma_0 k^2 + \Gamma_2 k^4) \hat{\varepsilon}. \quad [29]$$

Multiplying the second equation by \mathbf{k} and using the incompressibility condition implies that $\hat{\eta} = 0$ and, therefore,

$$\sigma(\mathbf{k}) = -(\alpha + \Gamma_0 k^2 + \Gamma_2 k^4). \quad [30]$$

Assuming $\Gamma_0 < 0$ and $\Gamma_2 > 0$, we find an unstable band of modes with $\sigma(\mathbf{k}) > 0$ for $k_-^2 < k^2 < k_+^2$, where

$$k_{\pm}^2 = \frac{|\Gamma_0|}{\Gamma_2} \left(\frac{1}{2} \pm \sqrt{\frac{1}{4} - \frac{\alpha \Gamma_2}{|\Gamma_0|^2}} \right) \quad [31]$$

provided that

$$4\alpha < |\Gamma_0|^2/\Gamma_2. \quad [32]$$

Note that for $\alpha < 0$ the isotropic state is generally unstable with respect to long-wave length (small- k) perturbations.

(ii) Stability of the ordered polar state \mathcal{S}_p . We next perform a similar analysis for the polar state (\mathbf{v}_0, p_0) , which exists for $\alpha < 0$. This state corresponds to all particles swimming in the same direction. In this case, when considering small deviations

$$\mathbf{v} = \mathbf{v}_0 + \varepsilon, \quad p = p_0 + \eta, \quad [33]$$

it is useful to distinguish perturbations perpendicular and parallel to \mathbf{v}_0 , by writing $\varepsilon = \varepsilon_{||} + \varepsilon_{\perp}$ where $\mathbf{v}_0 \cdot \varepsilon_{\perp} = 0$ and $\mathbf{v}_0 \cdot \varepsilon_{||} = v_0 \varepsilon_{||}$. Without loss of generality, we may choose \mathbf{v}_0 to point along the x -axis, $\mathbf{v}_0 = v_0 \mathbf{e}_x$. Adopting this convention, we have $\varepsilon_{||} = (\varepsilon_{||}, 0)$ and $\varepsilon_{\perp} = (0, \varepsilon_{\perp})$, and to leading order

$$|\mathbf{v}|^2 \simeq v_0^2 + 2v_0 \varepsilon_{||}. \quad [34]$$

Again considering exponential perturbations of the form

$$(\eta, \varepsilon_{||}, \varepsilon_{\perp}) = (\hat{\eta}, \hat{\varepsilon}_{||}, \hat{\varepsilon}_{\perp}) e^{i\mathbf{k} \cdot \mathbf{x} + \sigma t}, \quad [35]$$

we find in linear approximation

$$0 = \mathbf{k} \cdot \hat{\varepsilon}, \quad [36]$$

$$\sigma \hat{\varepsilon} = -i(\hat{\eta} - 2v_0 \lambda_1 \hat{\varepsilon}_{||}) \mathbf{k} + \mathbf{A} \hat{\varepsilon}, \quad [37]$$

where

$$\mathbf{A} = \begin{pmatrix} 2\alpha & 0 \\ 0 & 0 \end{pmatrix} - (\Gamma_0 k^2 + \Gamma_2 k^4 + i\lambda_0 k_x v_0) \mathbf{I} \quad [38]$$

with \mathbf{I} denoting the identity matrix. Multiplying Eq. [37] with $i\mathbf{k}$, and using the incompressibility condition [36], gives

$$\hat{\eta} = 2v_0\lambda_1\varepsilon_{||} - i\frac{\mathbf{k} \cdot (\mathbf{A}\hat{\varepsilon})}{k^2}. \quad [39]$$

Inserting this into Eq. [37] and defining $\mathbf{A}_\perp = \mathbf{\Pi}(\mathbf{k})\mathbf{A}$, where

$$\Pi_{ij}(\mathbf{k}) := \delta_{ij} - \frac{k_i k_j}{k^2} \quad [40]$$

is the orthogonal projector of \mathbf{k} , we obtain

$$\sigma\hat{\varepsilon} = \mathbf{A}_\perp\hat{\varepsilon}. \quad [41]$$

The eigenvalue spectrum of the matrix \mathbf{A}_\perp is given by

$$\sigma(\mathbf{k}) \in \left\{ 0, -\left(\Gamma_0 k^2 + \Gamma_2 k^4 - 2\alpha \frac{k_x^2}{k^2} \right) - i\lambda_0 v_0 k_x \right\}. \quad [42]$$

The zero eigenvalues correspond to the Goldstone modes. The non-zero eigenvalues have eigenvectors $(-k_y, k_x)$, implying that, for $\Gamma_0 < 0$, there will be a range of exponentially growing k -modes in the direction perpendicular to \mathbf{k} .

We may thus summarize: Eqs. [30] and [42] show that, for $\alpha < 0$ and $\Gamma_0 < 0$, the two fixed points become simultaneously unstable, indicating the existence of a quasi-stationary spatially inhomogeneous dynamic attractor. By contrast, for $\Gamma_0 > 0$ the polar state becomes stable, as evident from Eq. [42]. More generally, the above analysis suggests that the combination of the two Γ -terms is arguably the simplest linear way of constructing a \mathbf{v} -only theory with non-trivial stationary dynamics within the class of ‘standard’ partial differential equations. We note that, in principle, it would also be possible to generate similar instabilities by combining odd or fractional powers of k in Eqs. [30] and [42]; this would be somewhat similar to replacing the quartic Landau potential by a more general function of $|\mathbf{v}|$. However, when considering eigenvalue spectra based on odd or non-integer powers of k , the underlying dynamical equations in position space would correspond to fractional partial differential equations. One may speculate that such fractional models could potentially be useful for modeling active suspensions with long-range or other types of more complex interactions. The comparison with our quasi-2D experiments, however, illustrates that Eqs. [16] and [22] provide a useful continuum description of dense bacterial suspensions.

Guidance for Numerical Parameters Estimation. The minimal model from in Eqs. [16] and [22] features a relatively small number of parameters, which can be constrained by comparison with experiments. For $\alpha < 0$ the polar velocity $v_0 = \sqrt{|\alpha|/\beta}$ should be approximately equal to the swimming speed of a bacterium in suspension. Γ_0 and Γ_2 define characteristic length and velocity scales

$$\Lambda = \sqrt{\Gamma_2/|\Gamma_0|}, \quad V_\Gamma = \sqrt{|\Gamma_0|^3/\Gamma_2}, \quad [43]$$

that can be roughly estimated from the characteristic vortex size and swimming velocity of the bacteria, thereby yielding approximate values for Γ_0 and Γ_2 that can be used as starting points for systematic parameter scans in numerical simulations.

Furthermore, the parameter α defines a characteristic damping (acceleration) time-scale

$$\tau_\alpha = 1/|\alpha| \quad [44]$$

in the isotropic case $\alpha > 0$ (polar case $\alpha < 0$). To obtain turbulent states, this time scale τ_α must be much larger than the time scale for the growth of instabilities

$$\tau_T = \Gamma_2/|\Gamma_0|^2, \quad [45]$$

which roughly correspond to the maximum of the real part of $\sigma(\mathbf{k})$ in Eqs. [30] and [42]. Hence, the criterion for active mesoscale turbulence can be formulated as

$$R := \frac{\tau_\alpha}{\tau_T} = \frac{|\Gamma_0|^2}{\Gamma_2|\alpha|} \gg 1, \quad [46]$$

which is consistent with Eq. [32]. In this regime, simulation time steps must be chosen much smaller than τ_T .

As stated above, for pusher-type swimmers like *E. coli* or *B. subtilis*, the dimensionless nematic order parameter S should be negative [16]. Intuitively, negative values of S increase both the convective non-linearity (via λ_0) and the local pressure (via λ_1). In our simulations, we found that moderate values $|S| \sim (1 \div 3)$ typically produce good agreement with our experimental data.

Finally, the parameter β in the fourth-order term of the Landau potential determines the damping of large velocities. To reproduce the Gaussian velocity statistics observed in experiments, β must be chosen sufficiently small in simulations. It should be stressed that the quartic velocity potentials, which essentially arises from a small- $|\mathbf{v}|$ expansion, becomes inaccurate for large velocities. Therefore, one cannot expect that hydrodynamic models that are based on such Landau-type approximations correctly capture the tails of the velocity statistics in bacterial suspensions. Nevertheless, as our study shows, these models are able to describe the main phenomenological aspects of active meso-scale turbulence.

Simulation Parameters. In our 2D simulations of Eqs. [16] and [22], we use periodic boundary conditions and adopt characteristic units such that the length L of the quadratic simulation box is given by $L = \pi$ and the velocity scale by $V_\Gamma = \sqrt{|\Gamma_0|^3/\Gamma_2} = 1$. The remaining parameters are tuned such that the flow characteristics (number of vortices, spectral properties, etc.) in the simulated volume match the experimental quasi-2D data for *B. subtilis* as closely as possible. To compare simulation results with experiments, we assume that $v_0 \sim 35 \mu\text{m/s}$ in physical units while fixing the conversion factor for the box length L such that the typical vortex size in the experiments agrees with that in the simulations. For example, for the parameters used in Figs. 2-4 of the Main Text (which are listed in the Table below), the length of the simulation box corresponds to $L \sim 150 \mu\text{m}$, which is comparable to the experimental field of view and implies that simulation time is measured in units of $T_0 = (L/\pi)/V_\Gamma \sim 1.9$ s. Hence, one minute in real time equals a simulation period $T \sim 30$ in characteristic units. After systematically scanning a wide range of parameters, we found that the following values yield good agreement with the quasi-2D *B. subtilis* experiments:

parameter	rescaled value in simulations	value	units
box size L	π	150	μm
V_Γ	1	25	$\mu\text{m/s}$
α	-1	-0.5	$1/\text{s}$
β	0.5	4×10^{-4}	$\text{s}/\mu\text{m}^2$
Γ_0	-0.045	-53	$\mu\text{m}^2/\text{s}$
Γ_2	$ \Gamma_0 ^3$	245	$\mu\text{m}^4/\text{s}$
S	-2.5	-2.5	1

With these parameters, the continuum model correctly reproduces the main equal-time statistical quantifiers (see Fig. 3 and 4 in the Main Text) and also the approximately exponential decay of the two-time autocorrelations $\langle \mathbf{v}(t, \mathbf{r}) \mathbf{v}(t', \mathbf{r}) \rangle$ of the quasi-2D experimental data (see Fig. S9 below). For both experiments and simulations, the typical correlation time is of the order of 0.5 s which corresponds approximately to the typical vortex size (a few ℓ) divided by the polar speed v_0 .

Numerical Methods. To simulate the 2D continuum model with periodic boundary conditions, we used a pseudo-spectral algorithm as commonly employed in computational fluid dynamics [19]. The model equations were transformed into Fourier space and the resulting set of ordinary differential equations were solved numerically by an integrating factor method that solves the linear terms exactly [20]. The results were cross-checked with an implicit-explicit Euler integration [21]. In both schemes, nonlinear terms were treated carefully by implementing the 2/3-rule to suppress aliasing errors [22]. This means that, for quadratic nonlinearities, wave-vectors corresponding to wavelengths larger than 2/3 of the box size are set to zero and, similarly, for higher-order terms. Therefore, the effective spatial grid-size is smaller than the one used in the fluid solver. In our simulations, we tested different effective grid-sizes, ranging from 64×64 to 256×256 lattice points. Typical time steps used were of the order $\Delta t = 10^{-4}$ in dimensionless units as introduced above (specifically, $\Delta t = 2 \times 10^{-4}$ for the figures in the Main Text). To ensure that the flow vector fields remain divergence-free, the hydrodynamic pressure p is calculated using a pressure correction routine. Our fluid solver was written in Matlab and stability of the code was verified for a wide range of parameters.

Simulations were initiated with isotropic randomly chosen flow field configurations $\mathbf{v}(0, \mathbf{x})$ and were allowed to relax for 10^4 time steps, before data for the velocity fields were stored. Thereafter, snapshots were generated with a separation of 1000 time steps between successive outputs. In our statistical analysis we typically used data from ~ 900 snapshots.

1. Kirchhoff, T., Löwen, H., & Klein, R. (1996) Dynamical correlations in suspensions of charged rodlike macromolecules. *Phys. Rev. E* **53**, 5011–5022.
2. Drescher, K., Dunkel, J., Cisneros, L. H., Ganguly, S., & Goldstein, R. E. (2011) Fluid dynamics and noise in bacterial cell-cell and cell-surface scattering. *Proc. Natl. Acad. Sci. USA* **108**, 10940–10945.
3. Tirado, M. M., de la Torre, J. G., & Martinez, C. L. (1984) Comparison of theories for the translational and rotational diffusion coefficients of rod-like macromolecules. Application to short DNA fragments. *J. Chem. Phys.* **81**, 2047–2052.
4. Cisneros, L. H., Cortez, R., Dombrowski, C., Goldstein, R. E., & Kessler, J. O. (2007) Fluid dynamics of self-propelled micro-organisms, from individuals to concentrated populations. *Experiments in Fluids* **43**, 737–753.
5. Cisneros, L. H., Kessler, J. O., Ganguly, S., & Goldstein, R. E. (2011) Dynamics of swimming bacteria: Transition to directional order at high concentration. *Phys. Rev. E* **83**, 061907.
6. Zhang, H. P., Be'er, A., Smith, R. S., Florin, E., & Swinney, H. L. (2009) Swarming dynamics in bacterial colonies. *EPL* **87**, 48011.
7. Sokolov, A., Aranson, I. S., Kessler, J. O., & Goldstein, R. E. (2007) Concentration dependence of the collective dynamics of swimming bacteria. *Phys. Rev. Lett.* **98**, 158102.
8. Chen, X., Dong, X., Be'er, A., Swinney, H. L., & Zhang, H. P. (2012) Scale-invariant correlations in dynamic bacterial clusters. *Phys. Rev. Lett.* **108**, 148101.
9. Zhang, H. P., Be'er, A., Florin, E.-L., & Swinney, H. L. (2010) Collective motion and density fluctuations in bacterial colonies. *Proc. Natl. Acad. Sci. USA* **107**, 13626–13630.
10. Volfson, D., Cookson, S., Hasty, J., & Tsimring, L. S. (2008) Biomechanical ordering of dense cell populations. *Proc. Natl. Acad. Sci. USA* **105**, 15346–15351.

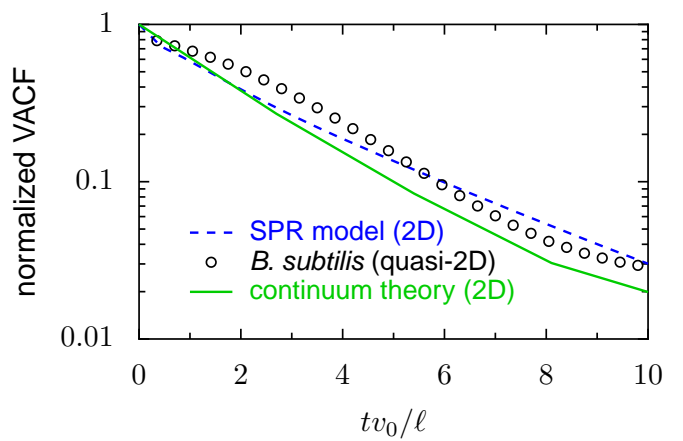


Fig. S9. The two-time velocity autocorrelation functions (VACFs) $\langle \mathbf{v}(t, \mathbf{r}) \mathbf{v}(t', \mathbf{r}) \rangle$, normalized by $\langle \mathbf{v}^2 \rangle$, decay approximately exponentially for both experimental and model data. To rescale the time-axis, we used for the SPR model the rod length ℓ and $v_0 = V$, where V is free rod speed as defined by Eq. [12], whereas for the experiments and the continuum theory we used the bacterial length $\ell = 4.8 \mu\text{m}$ and $v_0 = \sqrt{|\alpha|/\beta} = 35 \mu\text{m/s}$ as obtained from the parameters given in the Table above. The good quantitative agreement shows that the 2D continuum theory can reproduce not only the main characteristics of equal-time statistics (see Fig. 3 and 4 in the Main Text) but also the most relevant dynamical features of the quasi-2D *B. subtilis* experiments.

Supplementary Movie Information

Supplementary Movies S1-S6 represent results of the SPR simulations. Each of those movies shows the dynamics in a subsection of the total simulation volume (with comparable mean particle number) over the last 20% of the total simulations time interval. Simulation parameters are the same as in Fig. S2. Movies S7-S10 show representative movie data from quasi-2D and 3D experiments as used for the statistical analysis in the Main Text. Raw data and higher-resolution movies can be downloaded from <http://damtp.cam.ac.uk/user/gold/datarequests.html>

11. Toner, J & Tu, Y. (1995) Long-range order in a two-dimensional dynamical xy model: How birds fly together. *Phys. Rev. Lett.* **75**, 4326–4329.
12. Toner, J & Tu, Y. (1998) Flocks, herds, and schools: A quantitative theory of flocking. *Phys. Rev. E* **58**, 4828–4858.
13. Swift, J & Hohenberg, P. C. (1977) Hydrodynamic fluctuations at the convective instability. *Phys. Rev. A* **15**, 319–328.
14. Wolgemuth, C. W. (2008) Collective swimming and the dynamics of bacterial turbulence. *Biophys. J.* **95**, 1564–1574.
15. Ramaswamy, S. (2002) Hydrodynamic fluctuations and instabilities in ordered suspensions of self-propelled particles. *Phys. Rev. Lett.* **89**, 058101.
16. Pedley, T. J. (2010) Collective behaviour of swimming micro-organisms. *Experimental Mechanics* **50**, 1293–1301.
17. de Gennes, P. G & Prost, J. (1995) *The Physics of Liquid Crystals*. (Oxford University Press, Oxford) Vol. 2.
18. Baskaran, A & Marchetti, M. C. (2008) Hydrodynamics of self-propelled hard rods. *Phys. Rev. E* **77**, 011920.
19. Gottlieb, D & Orszag, S. A. (1977) *Numerical analysis of spectral methods: Theory and applications*. (SIAM, Philadelphia).
20. Pedrosa, J., Hoyuelos, M., & Martel, C. (2008) Numerical validation of the complex swift-hohenberg equation for lasers. *Eur. Phys. J. B* **66**, 525–530.
21. Ascher, U. M., Ruuth, S. J., & Wetton, B. T. R. (1996) Implicit-explicit methods for time-dependent partial differential equations. *SIAM J. Numer. Anal.* **32**, 797–823.
22. Canuto, C., Hussaini, M. Y., Quarteroni, A., & Zang, T. A. (2006) *Spectral methods: fundamentals in single domains*. (Springer, Berlin).